Applied Mathematical Modelling 36 (2012) 5466–5481

Contents lists available at SciVerse ScienceDirect

Applied Mathematical Modelling

journal homepage: www.elsevier.com/locate/apm

Investigation on polynomial integrators for time-domain electromagnetics using a high-order discontinuous Galerkin method

H. Fahs [1]

XLIM Institute, OSA Department, UMR CNRS 6172, 123 Avenue Albert Thomas, 87060 Limoges Cedex, France

ARTICLE INFO

Article history:
Received 25 May 2011
Received in revised form 18 December 2011
Accepted 21 December 2011
Available online 9 January 2012

Keywords:
Maxwell's equations
Discontinuous Galerkin method
Time-stepping schemes
Faber polynomials

ABSTRACT

In this work, we investigate the application of polynomial integrators in a high-order discontinuous Galerkin method for solving the time-domain Maxwell equations. After the spatial discretization, we obtain a time-continuous system of ordinary differential equations of the form, $\partial_t \mathbb{Y}(t) = \mathcal{H}\mathbb{Y}(t)$, where $\mathbb{Y}(t)$ is the electromagnetic field, $\mathcal{H}$ is a matrix containing the spatial derivatives, and t is the time variable. The formal solution is written as the exponential evolution operator, $\exp(t\mathcal{H})$, acting on a vector representing the initial condition of the electromagnetic field. The polynomial integrators are based on the approximation of $\exp(t\mathcal{H})$ by an expansion of the form $\sum_{m=0}^{\infty} g_m(t)P_m(\mathcal{H})$, where $g_m(t)$ is a function of time and $P_m(\mathcal{H})$ is a polynomial of order m satisfying a short recursion. We introduce a general family of expansions of $\exp(t\mathcal{H})$ based on Faber polynomials. This family of expansions is suitable for non-Hermitian matrices, and consequently the proposed integrators can handle absorbing media and conductive materials. We discuss the efficient implementation of this technique, and based on some test problems, we compare the virtues and shortcomings of the algorithm. We also demonstrate how this scheme provides an efficient alternative to standard explicit integrators.

1. Introduction

Nowadays, a variety of methods exist for the numerical treatment of the time-domain Maxwell equations, ranging from the well established and still prominent FDTD methods based on Yee's scheme [1], to the more recent finite element time domain (FETD) [2], and discontinuous Galerkin time domain (DGTD) methods [3]. The use of unstructured meshes is an intrinsic feature of the latter methods which can easily deal with complex geometries and heterogeneous propagation media. In this paper we are interested in discontinuous Galerkin (DG) methods which are a class of finite element methods (FE) based on completely discontinuous piecewise polynomial spaces for the numerical solution and the test functions. For the same order of accuracy, DG methods require more degrees of freedom than continuous FE methods. To obtain highly accurate and stable DG methods, suitable numerical fluxes need to be designed over elemental interfaces. The construction of such numerical fluxes can be done in many different ways that are closely related to the particular equations [4]. The DG method has become very popular in recent years for solving electromagnetic (EM) wave propagation problems [5]. It has several distinct advantages. We refer to the lecture notes [6] and the textbook [3] for details and history of the DG method. In particular, the DG method is flexible with regards to the choice of the time-stepping scheme. One may combine the DG spatial discretization with any explicit [7] or implicit [8] time schemes, or even a blending between these two schemes [9], provided that the resulting scheme will be stable.

[1] Present address: University Paris-Est Marne-la-Vallée, LAMA Laboratory, 5 boulevard Descartes, 77454 Marne-la-Vallée Cedex 2, France.
E-mail address: Hassan.Fahs@gmail.com

0307-904X/$ - see front matter © 2011 Elsevier Inc. All rights reserved.
doi:10.1016/j.apm.2011.12.055

The DGTD methods for Maxwell's equations are derived in two stages. First, the spatial operators are discretized on an appropriate mesh covering the spatial domain, together with the accompanying boundary conditions. This leads to a time-continuous, semi discrete problem in the form of an initial-value problem for a system of first-order ordinary differential equations (ODEs), see Section 3,

$$\partial_t \mathbb{Y}(t) = \mathcal{H}\mathbb{Y}(t), \tag{1}$$

where $\mathbb{Y}(t)$ is the EM field and $\mathcal{H}$ is a real time-independent matrix arising from the DG discretization and depends on the spatial configuration, material parameters and boundary conditions. Second, a numerical integration method for this ODE system is chosen, which turns the semi-discrete solution into the desired fully discrete solution on the chosen space–time grid. In this paper we focus on the second numerical integration stage, as in [10,9]. The solution of Eq. (1) can be formally written as $\mathbb{Y}(t) = \Phi(t)\mathbb{Y}(0)$, where $\mathbb{Y}(0)$ represents the initial state of the EM field and $\Phi(t) = \exp(t\mathcal{H})$ is the time evolution operator. The construction of high-order time integrators for problems of type Eq. (1) is usually based on an approximation of the operator $\Phi(t)$. These methods employ various algorithms to compute an exponential and other functions of the matrix $\mathcal{H}$. Most frequently, these algorithms are based on Taylor or Padé expansions. Although in principle these expansions are convergent, in practice they are very inaccurate when $\|t\mathcal{H}\|$ is large [11]. Other integration schemes use the Suzuki product formula or the split operator (SPO) method [12] which facilitates the implementation of higher-order accurate schemes with very low dispersion even for large time steps. Although these schemes are unconditionally stable, they rely on rewriting Maxwell's equations as an operator-equation with a strictly skew-symmetric matrix $\mathcal{H}$ and, therefore, are not convenient for absorbing or dispersive media. A more general approach to approximating an exponential or other functions of a large matrix comes from computational linear algebra. van der Vorst [13] was amongst the first to be aware of the potential of using established methods, such as the Lanczos or Arnoldi algorithms. For Hermitian matrices, the Krylov-subspace technique based on the Arnoldi process is highly accurate and efficient. Min and Fischer [14] applied the Krylov algorithm to a spectral-element DG method for Maxwell's equations and very accurate results were obtained compared to a fourth-order Runge–Kutta method. For non-Hermitian matrices, the Krylov technique is usually combined with the SPO method in order to treat absorbing media. While the unconditional stability is maintained, the accuracy is limited by the accuracy of the SPO approximation rather than by the dimension of the Krylov space, see [15] for a recent discussion on this issue.

Another class for calculating the operator $\Phi(t)$ for large matrix $\mathcal{H}$ consists to expand it in the form $\Phi(t) = \sum_{m=0}^{\infty} g_m(t) P_m(\mathcal{H})$, where $g_m(t)$ is a function of time and $P_m(\mathcal{H})$ is a polynomial of order m. This class will be referred to as *polynomial expansion method* (PEM) which is the subject of this paper. The PEM has been widely used in the calculation of dynamics and/or spectral properties of large quantum systems with great success [16–18]. In 1984 Tal-Ezer and Kosloff [16] proposed an expansion in terms of first-kind Chebyshev polynomials (CH-scheme) for solving the Shrödinger wave equation in one and two dimensions. The authors tested the method with the simple harmonic oscillator and the problem of scattering from a metal surface; very accurate results were obtained with an efficiency six times higher compared to the conventional scheme. A detailed comparison of the CH-scheme with various propagation schemes, was performed by Leforestier et al. [17] who showed that the CH-scheme offers an accurate and flexible alternative to other existing techniques for propagating the time-dependent Shrödinger equation. Since Maxwell's equations can be cast in the form of the Schrödinger equation, it is then natural to extend time-domain methods of quantum mechanics to numerical electrodynamics. For instance, the CH-scheme has been recently applied to electromagnetic [19], seismic [20] and acoustic [21] wave propagations in the context of FDTD methods; very accurate results were obtained for long time simulations compared to the Yee's algorithm and the SPO algorithm. While the CH-scheme is the most frequently used method, other expansions based on Legendre polynomials have also been introduced to study dynamics of large quantum systems [18]. These expansions provide similar accuracy compared to the CH-scheme. However, all PEMs cited above are consequently suited for Hermitian matrices, i.e., with real or purely imaginary eigenvalues. For non-Hermitian matrices, when the spectrum is defined in the complex plane, the Faber polynomials are more appropriate, and their use has been proposed by Moret and Novati [22]. The Faber approximation method has been applied to quantum scattering problems [23] to compute the causal Green's function for the Schrödinger equation. The Faber polynomial approximation of the exponential of a non-Hermitian operator has also been used to solve the initial value problem in electrodynamics of passive media [24] and for the Liouville-von Neumann equation that describes the time evolution of the density matrix in statistical systems [25,26]. As mentioned above, PEM has been extensively used in quantum electrodynamics, but to our knowledge, it has never been used for integrating the Maxwell equations using a DG method. This is the main topic of this paper.

The main purpose of this paper is to investigate the capabilities of PEM as a time-integration scheme for solving the time-dependent Maxwell equations with a high-order DG method. Below we will (i) describe the ideas behind constructing polynomial integrators, (ii) introduce a general family of integrators based on Faber polynomial expansions, (iii) discuss the efficient implementation of this technique, and (iv) based on some test problems, compare the virtues and shortcomings of the algorithm and provide guidance as to what computational savings one can expect compared to standard explicit methods. The rest of the paper is organized as follows. Section 2 recalls the Maxwell system and its DG discretization. In Section 3, we show that the solution of the Maxwell equations can be written in the form of Eq. (1). In this section we also give the basic idea of the polynomial expansion approach for the approximation of the time evolution operator. In Section 4, we construct expansions based on Faber polynomials that are able to treat absorbing media and conductive materials. Then, in Section 5, we present numerical results for several test cases. Finally, Section 6 contains a few concluding remarks and ideas for future works.

2. Governing equations and spatial discretization

The evolution of a time-dependent electromagnetic field $\boldsymbol{E}(\boldsymbol{x},t),\ \boldsymbol{H}(\boldsymbol{x},t)$ propagating through a linear isotropic medium is determined by Maxwell's equations

$$\varepsilon\partial_t\boldsymbol{E} = -\sigma\boldsymbol{E} + \nabla\times\boldsymbol{H}, \quad \mu\partial_t\boldsymbol{H} = -\nabla\times\boldsymbol{E}, \tag{2}$$

where $\varepsilon(\boldsymbol{x}),\ \mu(\boldsymbol{x})$ and $\sigma(\boldsymbol{x})$ are respectively the permittivity, the permeability and the conductivity of the medium. These equations are set and solved on a bounded open domain Ω of $\mathbb{R}^d,\ d \geqslant 1$. On the boundary $\partial\Omega = \Gamma_a \cup \Gamma_m$, we impose the following boundary conditions: a perfect electric conductor (PEC) condition: $\boldsymbol{n}\times\boldsymbol{E} = 0$ on Γ_m and/or a Silver-Müller absorbing condition: $\mathcal{L}(\boldsymbol{E},\boldsymbol{H}) = \mathcal{L}(\boldsymbol{E}_{\text{inc}},\ \boldsymbol{H}_{\text{inc}})$ on Γ_a where $\mathcal{L}(\boldsymbol{E},\boldsymbol{H}) = \boldsymbol{n}\times\boldsymbol{E} + c\mu\boldsymbol{n}\times(\boldsymbol{n}\times\boldsymbol{H})$. Here $\boldsymbol{n}$ denotes the unit outward normal to $\partial\Omega,\ c = 1/\sqrt{\varepsilon\mu}$ is the speed of propagation and $(\boldsymbol{E}_{\text{inc}},\boldsymbol{H}_{\text{inc}})$ is a given incident field.

We shall now discretize Maxwell's equations in space using the central DG method [10]. First, we consider a regular or r-irregular partition $\mathcal{T}_h$ of Ω into a collection of non-overlapping d-simplices or elements τ_i. Thus a $(d-1)$-dimensional face of each element τ_i in $\mathcal{T}_h$ is allowed to contain at most r hanging (irregular) nodes. We shall suppose that the family of partitions $\mathcal{T}_h$ is shape-regular and that each $\tau_i \in \mathcal{T}_h$ is the image, under a smooth bijective map Ψ_{τ_i}, of a fixed master element τ_r; that is, $\tau_i = \Psi_{\tau_i}(\tau_r)$ for all $\tau_i \in \mathcal{T}_h$, where τ_r is the open unit simplex in $\mathbb{R}^d$. Within this construction we allow for elements τ_i with curved edges or faces. For an integer $p \geqslant 1$, we denote by $[\mathbb{P}_p(\tau_r)]^d$ the space of d-dimensional nodal polynomials of degree at most p on τ_r. The dimension $N(p,d)$ of this space depends on the order p and on the spatial dimension d and is given by $N(p,d) = (p+d)!/p!d!$. Then, to each $\tau_i \in \mathcal{T}_h$ we assign an integer $p_i \geqslant 1$ that is the local polynomial degree inside τ_i; collecting the p_i and Ψ_{τ_i} in the vectors $\boldsymbol{p} = \{p_i : \tau_i \in \mathcal{T}_h\}$ and $\boldsymbol{\Psi} = \{\Psi_{\tau_i} : \tau_i \in \mathcal{T}_h\}$, respectively, we seek approximate solutions to Eq. (2) in the finite element space

$$V_{\boldsymbol{p}}(\Omega,\mathcal{T}_h,\boldsymbol{\Psi}) = \{\boldsymbol{u} \in [L^2(\Omega)]^d : u_{k|\tau_i}\circ\Psi_{\tau_i} \in [\mathbb{P}_{p_i}(\tau_r)]^d, k = 1,\ldots,d, \forall\tau_i \in \mathcal{T}_h\},$$

where $[L^2(\Omega)]^d$ is the space of square integrable functions on Ω. For each element τ_i, the parameters ε_i,μ_i and σ_i denote respectively the local permittivity, permeability and conductivity of the medium, which are assumed constant inside the element τ_i. For two distinct elements τ_i and τ_k in $\mathcal{T}_h$, the intersection $a_{ik} = \tau_i \cap \tau_k$ is a $(d-1)$-dimensional face in $\mathcal{T}_h$ (a convex polyhedron), with unitary normal vector $\boldsymbol{n}_{ik}$, oriented from τ_i towards τ_k. For the boundary faces, the index k corresponds to a fictitious element outside the domain. Finally, we denote by $\mathcal{F}^{\text{int}}, \mathcal{F}^m$ and $\mathcal{F}^a$ the union of all interior, metallic and absorbing faces of $\mathcal{T}_h$, respectively, and set $\mathcal{F} = \mathcal{F}^{\text{int}} \cup \mathcal{F}^m \cup \mathcal{F}^a$.

Following the DG approach, the electric and magnetic fields are approximated inside each finite element τ_i by a linear combination of basis functions $\varphi_{ij}(\boldsymbol{x})$ with support τ_i and with time-dependent coefficient functions $E_{ij}(t)$ and $H_{ij}(t)$ as follows

$$\boldsymbol{E}_i = \sum_{1\leqslant j\leqslant N_i} E_{ij}(t)\varphi_{ij}(\boldsymbol{x}), \quad \boldsymbol{H}_i = \sum_{1\leqslant j\leqslant N_i} H_{ij}(t)\varphi_{ij}(\boldsymbol{x}). \tag{3}$$

Here, the index j indicates the jth basis function and $N_i = N(p_i,d)$ denotes the local number of degrees of freedom inside τ_i. As usual for DG schemes, the Maxwell system, Eq. (2), is multiplied by a test function $\varphi \in \text{span}\{\varphi_{ij},\ 1 \leqslant j \leqslant N_i\}$ and integrated over each single element τ_i. After integration by parts, inserting the DG approximation, Eq. (3), and after applying a centered numerical flux in the boundary integrals, the semi-discrete formulation of the scheme in the physical element τ_i reads as [10]

$$\begin{aligned}
\int_{\tau_i}\varphi\cdot\varepsilon_i\partial_t\boldsymbol{E}_i &= -\int_{\tau_i}\varphi\cdot\sigma_i\boldsymbol{E}_i + \frac{1}{2}\int_{\tau_i}(\nabla\times\varphi\cdot\boldsymbol{H}_i + \nabla\times\boldsymbol{H}_i\cdot\varphi) - \frac{1}{2}\sum_{a_{ik}\in\mathcal{F}}\int_{a_{ik}}\varphi\cdot(\boldsymbol{H}_k\times\boldsymbol{n}_{ik}),\\
\int_{\tau_i}\varphi\cdot\mu_i\partial_t\boldsymbol{H}_i &= -\frac{1}{2}\int_{\tau_i}(\nabla\times\varphi\cdot\boldsymbol{E}_i + \nabla\times\boldsymbol{E}_i\cdot\varphi) + \frac{1}{2}\sum_{a_{ik}\in\mathcal{F}}\int_{a_{ik}}\varphi\cdot(\boldsymbol{E}_k\times\boldsymbol{n}_{ik}).
\end{aligned} \tag{4}$$

The boundary conditions are dealt with *weakly*, in the sense that the traces on a_{ik} of fictitious fields $\boldsymbol{E}_k$ and $\boldsymbol{H}_k$ are used for the computation of numerical fluxes in Eq. (4) for the boundary element τ_i. More precisely, for $a_{ik} \in \Gamma_m$ we set $\boldsymbol{E}_k = -\boldsymbol{E}_i$ and $\boldsymbol{H}_k = \boldsymbol{H}_i$. Concerning absorbing faces $a_{ik} \in \Gamma_a$, we propose the fictitious fields $\boldsymbol{E}_k = c_i\varepsilon_i(\boldsymbol{n}_{ik}\times\boldsymbol{E}_i)$ and symmetrically $\boldsymbol{H}_k = -c_i\mu_i(\boldsymbol{n}_{ik}\times\boldsymbol{H}_i)$, where $c_i = 1/\sqrt{\varepsilon_i\mu_i}$. These values correspond to upwind fluxes at the absorbing boundary, based on the hyperbolic nature of the Maxwell system. Eq. (4) can be rewritten in terms of scalar unknowns inside each element τ_i. We now denote by $\bar{\mathbf{E}}_i$ and $\bar{\mathbf{H}}_i$, respectively, the column vectors $(E_{ij})_{1\leqslant j\leqslant N_i}$ and $(H_{ij})_{1\leqslant j\leqslant N_i}$. Then, Eq. (4) is equivalent to

$$\begin{aligned}
\mathrm{M}_i^{\varepsilon}\partial_t\bar{\mathbf{E}}_i &= -\mathrm{M}_i^{\sigma}\bar{\mathbf{E}}_i + \mathrm{K}_i\bar{\mathbf{H}}_i - \sum_{a_{ik}\in\mathcal{F}^{\text{int}}}\mathrm{S}_{ik}\bar{\mathbf{H}}_k - \sum_{a_{ik}\in\mathcal{F}^m}\mathrm{S}_{ik}\bar{\mathbf{H}}_i + \sum_{a_{ik}\in\mathcal{F}^a}\mathrm{S}_{ik}^{\varepsilon}\bar{\mathbf{E}}_i,\\
\mathrm{M}_i^{\mu}\partial_t\bar{\mathbf{H}}_i &= -\mathrm{K}_i\bar{\mathbf{E}}_i + \sum_{a_{ik}\in\mathcal{F}^{\text{int}}}\mathrm{S}_{ik}\bar{\mathbf{E}}_k - \sum_{a_{ik}\in\mathcal{F}^m}\mathrm{S}_{ik}\bar{\mathbf{E}}_i + \sum_{a_{ik}\in\mathcal{F}^a}\mathrm{S}_{ik}^{\mu}\bar{\mathbf{H}}_i,
\end{aligned} \tag{5}$$

where the mass matrices $\mathrm{M}_i^{\varkappa}$ ($\varkappa$ stands for ε or, μ or, σ), the stiffness matrix K_i (all of size $N_i\times N_i$) and the $N_i\times N_k$ flux matrices S_{ik} and S_{ik}^{κ} (κ stands for ε or μ) are given by

$$
\begin{aligned}
&(\mathrm{M}_i^{\varkappa})_{jl} = \varkappa_i \int_{\tau_i} \varphi_{ij} \cdot \varphi_{il}, \quad (\mathrm{K}_i)_{jl} = \frac{1}{2} \int_{\tau_i} \varphi_{ij} \cdot \nabla \times \varphi_{il} + \varphi_{il} \cdot \nabla \times \varphi_{ij}, \\
&(\mathrm{S}_{ik})_{jl} = \frac{1}{2} \int_{a_{ik}} \varphi_{ij} \cdot (\varphi_{kl} \times \boldsymbol{n}_{ik}), \quad (\mathrm{S}_{ik}^{\kappa})_{jl} = \frac{1}{2} c_i \kappa_i \int_{a_{ik}} (\varphi_{ij} \times \boldsymbol{n}_{ik}) \cdot (\varphi_{kl} \times \boldsymbol{n}_{ik}).
\end{aligned} \tag{6}
$$

These matrices are evaluated by a numerical integration scheme based on a family of high-order cubature formulas for line, surface, and volume integrals. For complete details on this issue, see [10,27].

3. Polynomial integrators applied to discrete Maxwell's equations

In some cases, the discretization of Maxwell's equations actually leads to a Hamiltonian system of ODEs: it is indeed the case for some FDTD methods [19], more generally for FETD methods [28], and also for the case considered here: DGTD methods with totally centered fluxes. In this section, we will describe the main idea behind the polynomial integrators and will explain how to apply them to the Hamiltonian form of the discretized Maxwell equations.

The set of local system of ODEs for each τ_i, Eq. (5), can be formally transformed in a global system. To this end, we suppose that all electric (resp. magnetic) unknowns are gathered in a column vector $\mathbb{E}$ (resp. $\mathbb{H}$) of size $N_g = \sum_{i=1}^{n_e} N_i$ where n_e stands for the number of elements in $\mathcal{T}_h$. Then system (5) can be rewritten as

$$
\begin{aligned}
&\mathbb{M}_\varepsilon \partial_t \mathbb{E} = -\mathbb{M}_\sigma \mathbb{E} + \mathbb{K}\mathbb{H} - \mathbb{A}\mathbb{H} - \mathbb{B}\mathbb{H} + \mathbb{C}_\varepsilon \mathbb{E}, \\
&\mathbb{M}_\mu \partial_t \mathbb{H} = -\mathbb{K}\mathbb{E} + \mathbb{A}\mathbb{E} - \mathbb{B}\mathbb{E} + \mathbb{C}_\mu \mathbb{H},
\end{aligned} \tag{7}
$$

where we have used the following definitions and properties: (a) $\mathbb{M}_\varepsilon, \mathbb{M}_\mu, \mathbb{M}_\sigma$ and $\mathbb{K}$ are $N_g \times N_g$ block diagonal matrices with diagonal blocks equal to $\mathrm{M}_i^{\varepsilon}$, M_i^{μ}, M_i^{σ} and K_i respectively. $\mathbb{M}_\varepsilon$, $\mathbb{M}_\mu$ and $\mathbb{M}_\sigma$ are symmetric positive definite matrices, and $\mathbb{K}$ is a symmetric matrix; (b) $\mathbb{A}$ is also a $N_g \times N_g$ symmetric block sparse matrix, whose non-zero blocks are equal to S_{ik} when $a_{ik} \in \mathcal{F}^{\mathrm{int}}$; (c) $\mathbb{B}$ is a $N_g \times N_g$ skew-symmetric block diagonal matrix, whose non-zero blocks are equal to S_{ik} when $a_{ik} \in \mathcal{F}^{m}$; and (d) $\mathbb{C}_\varepsilon$ and $\mathbb{C}_\mu$ are $N_g \times N_g$ symmetric block diagonal matrices, whose non-zero blocks are equal to $\mathrm{S}_{ik}^{\varepsilon}$ and S_{ik}^{μ} respectively, when $a_{ik} \in \mathcal{F}^{a}$. Let $\mathbb{S} = \mathbb{K} - \mathbb{A} - \mathbb{B}$; the system (7) rewrites as

$$
\partial_t \begin{pmatrix} \mathbb{M}_\varepsilon \mathbb{E} \\ \mathbb{M}_\mu \mathbb{H} \end{pmatrix} = \begin{pmatrix} \mathbb{C}_\varepsilon - \mathbb{M}_\sigma & \mathbb{S} \\ -\mathbb{S}^\dagger & \mathbb{C}_\mu \end{pmatrix} \begin{pmatrix} \mathbb{E} \\ \mathbb{H} \end{pmatrix}, \tag{8}
$$

where the dagger symbol stands for the conjugate transpose. Introducing the scaled fields $\tilde{\mathbb{E}} = \mathbb{M}_\varepsilon^{1/2}\mathbb{E}$, $\tilde{\mathbb{H}} = \mathbb{M}_\mu^{1/2}\mathbb{H}$, and writing $\mathbb{Y} = (\tilde{\mathbb{E}}, \tilde{\mathbb{H}})^\dagger$, Eq. (8) reads as

$$
\partial_t \mathbb{Y}(t) = \mathcal{H}\mathbb{Y}(t), \quad \text{with } \mathcal{H} = \begin{pmatrix} \tilde{\mathbb{C}}_{\varepsilon,\sigma} & \tilde{\mathbb{S}} \\ -\tilde{\mathbb{S}}^\dagger & \tilde{\mathbb{C}}_\mu \end{pmatrix}, \tag{9}
$$

where $\tilde{\mathbb{S}} = \mathbb{M}_\varepsilon^{-1/2}\mathbb{S}\mathbb{M}_\mu^{-1/2}$, $\tilde{\mathbb{C}}_{\varepsilon,\sigma} = \mathbb{M}_\varepsilon^{-1/2}(\mathbb{C}_\varepsilon - \mathbb{M}_\sigma)\mathbb{M}_\varepsilon^{-1/2}$, $\tilde{\mathbb{C}}_\mu = \mathbb{M}_\mu^{-1/2}\mathbb{C}_\mu\mathbb{M}_\mu^{-1/2}$, and the $2N_g \times 2N_g$ matrix $\mathcal{H}$ depends only on the spatial configuration. Eq. (9) is called the Hamiltonian form of the Maxwell equations, where $\mathcal{H}$ is the matrix Hamiltonian. For non-absorbing media and/or non-conducting materials ($\sigma = 0$), the matrix $\mathcal{H}$ is skew-symmetric, otherwise, it is unsymmetric. The formal solution of Eq. (9) is given by

$$
\mathbb{Y}(t) = \exp(t\mathcal{H})\mathbb{Y}(0) \equiv \Phi(t)\mathbb{Y}(0), \tag{10}
$$

where $\mathbb{Y}(0)$ represents the initial state of the EM field and the operator $\Phi(t) = \exp(t\mathcal{H})$ determines its time evolution matrix. We consider to solve Eq. (10) on a discrete time grid $\{t^n = n\tau, n = 0, 1, \ldots\}$, where τ is the fixed time step, and denote $\mathbb{Y}^n = \mathbb{Y}(t^n)$. The time discrete solution of Eq. (10) is given by

$$
\mathbb{Y}^{n+1} = \Phi(\tau)\mathbb{Y}^n. \tag{11}
$$

The construction of explicit polynomial integrators for problems of type Eq. (9) is based on the approximation of the time evolution operator $\Phi(\tau)$, which can be expressed in a *degenerate kernel* form

$$
\Phi(\tau) = \sum_{m=0}^{\infty} g_m(\tau) P_m(\mathcal{H}), \tag{12}
$$

where $P_m(\mathcal{H})$ is a polynomial of order m and $g_m(t)$ is a function of time. In most cases the polynomials $P_m(\mathcal{H})$ satisfy a three-term recurrence formula in the form

$$
P_{m+1}(\mathcal{H}) = (a_m\mathcal{H} + b_m)P_m(\mathcal{H}) + c_m P_{m-1}(\mathcal{H}), \tag{13}
$$

where the coefficients a_m, b_m and c_m depend on P_m and its order m. Thus, to find the vector $\mathbb{Y}^{n+1}$, we just need to sum successively the terms of the series (12), using Eq. (13) for calculation of the subsequent terms, until we reach some predefined value M of m, which can be determined by the required precision. The number M of terms in the sum depends on the polynomial used and on the size of the time step for which the propagator is needed.

In what follows, we are performing formal manipulations using functions of the matrix $\mathcal{H}$. All these functions are defined by the spectral decomposition [11]

$$f(\mathcal{H})\mathbb{Y}^n = \sum_{l=0}^{N} \boldsymbol{w}_l f(\lambda_l)\langle \boldsymbol{w}_l^\dagger, \mathbb{Y}^n\rangle, \tag{14}$$

where $\langle \boldsymbol{x},\boldsymbol{y}\rangle = \boldsymbol{x}^\dagger \boldsymbol{y}$ denotes the inner product of the vectors $\boldsymbol{x}$ and $\boldsymbol{y}$, $\boldsymbol{w}_l$ is an eigenfunction of $\mathcal{H}$ corresponding to the eigenvalue λ_l, and N is the dimension of spectrum of $\mathcal{H}$. If we choose $f(\mathcal{H}) = \exp(\tau\mathcal{H})$ in Eq. (14) and in the resulting expression we replace $\exp(\tau\mathcal{H})$ with the right-hand side of Eq. (12), we obtain

$$\exp(\tau\mathcal{H})\mathbb{Y}^n = \sum_{l=0}^{N} \boldsymbol{w}_l \sum_{m=0}^{\infty} g_m(\tau) P_m(\lambda_l)\langle \boldsymbol{w}_l^\dagger, \mathbb{Y}^n\rangle. \tag{15}$$

Interchanging the sums and using the definition, $P_m(\mathcal{H})\mathbb{Y}^n = \sum_{l=0}^{N} \boldsymbol{w}_l P_m(\lambda_l)\langle \boldsymbol{w}_l^\dagger, \mathbb{Y}^n\rangle$, allows us to write Eq. (15) as

$$\exp(\tau\mathcal{H})\mathbb{Y}^n = \sum_{m=0}^{\infty} g_m(\tau) P_m(\mathcal{H})\mathbb{Y}^n. \tag{16}$$

The right-hand side of Eq. (16) is now well defined, since there is not ambiguity in the meaning of matrix polynomials. However, since we use the spectral decomposition in the derivation, we must make sure that the polynomial $P_m(\lambda_l)$ is well defined. We will clarify this issue in the next sections. Now, assuming $\exp(\tau\mathcal{H})\mathbb{Y}^n$ has the following polynomial approximation of order M

$$\exp(\tau\mathcal{H})\mathbb{Y}^n \approx \sum_{m=0}^{M} g_m(\tau) P_m(\mathcal{H})\mathbb{Y}^n, \tag{17}$$

the following algorithm can be used to compute an approximation to $\exp(\tau\mathcal{H})\mathbb{Y}^n$:

Algorithm 1. Approximating $\exp(\tau\mathcal{H})\mathbb{Y}^n$ by polynomial expansions

Input: the fixed time step τ
1: Compute the truncation order M
2: $\boldsymbol{p}_0 = P_0(\mathcal{H})\mathbb{Y}^n$; $\boldsymbol{p}_1 = P_1(\mathcal{H})\mathbb{Y}^n$
3: $\boldsymbol{z}_1 = g_0(\tau)\boldsymbol{p}_0 + g_1(\tau)\boldsymbol{p}_1$
4: **for** $m = 1$ **to** $M - 1$ **do**
5: $\quad \boldsymbol{p}_{m+1} = a_m\mathcal{H}\boldsymbol{p}_m + b_m\boldsymbol{p}_m + c_m\boldsymbol{p}_{m-1}$
6: $\quad \boldsymbol{z}_{m+1} = \boldsymbol{z}_m + g_{m+1}(\tau)\boldsymbol{p}_{m+1}$
7: **end for**
8: **return** $\boldsymbol{z}_M \approx \exp(\tau\mathcal{H})\mathbb{Y}^n$

The Algorithm 1 uses Eq. (13) in line 5 and Eq. (17) in lines 3 and 6. If $\mathcal{H}$ is a $2N_g \times 2N_g$ matrix with $Nz(\mathcal{H})$ non-zero entries, then Algorithm 1 entails a computational cost of about $14N_g + 2Nz(\mathcal{H})$ operations per pass through the for-loop. Two vectors are needed to store $\boldsymbol{p}_m$ and $\boldsymbol{p}_{m-1}$. These are exchanged to the pair $\boldsymbol{p}_m$, $\boldsymbol{p}_{m+1}$ in the next step, which can be carried out in a constant number of operations by redirecting pointers rather than copying data. Another vector is needed to perform the matrix–vector (matvec) product $\mathcal{H}\boldsymbol{p}_m$ and another one to store the solution $\boldsymbol{z}_M$. This brings the total number of vectors to four and the computational work per time step to M matvecs.

Finally, it is worth noting that the polynomial integrator can be used as one-step method by getting the solution at the final time directly from the initial data. It can also be used as a marching scheme if one is interested in intermediate results (e.g., for comparisons with standard leap-frog or Runge–Kutta schemes). The size of the time step depends only on the information one wants to get out of the numerical procedure. The parameter M is then determined accordingly. The refinement of the scheme is then based on increasing the parameter M and not by decreasing the time step.

4. Faber polynomial integrators

As mentioned in the introduction, the Chebyshev polynomial integrator is, in general, well-suited only when the Hamiltonian matrix $\mathcal{H}$ in Eq. (9) is skew-symmetric, that is, when the boundaries of the domain are assumed to be PEC and the material is non-conductive. In this section we discuss the modifications required to extend the polynomial integrator schemes to include the treatment of absorbing boundaries (i.e., $\Gamma_a \neq \emptyset$) and/or non-conductive materials (i.e., $\mathbb{M}_\sigma \neq 0$). We shall construct time integrators based on the development of $\Phi(\tau)$ in a series of Faber polynomials which are generally appropriate when the eigenvalues of $\mathcal{H}$ are defined in the complex plane. In the remainder of this paper, τ refers to the normalized time step which is related to the physical time step, δt, as $\delta t = \tau/c_0$, where τ has units of meters (m) and δt has units of seconds (s). Here $c_0 = (\varepsilon_0\mu_0)^{-1/2} \approx 3 \times 10^8$ m/s represents the dimensional vacuum speed of light with ε_0 and μ_0 being the vacuum permittivity and permeability, respectively.

4.1. Motivating example

Let us begin with an example to illustrate the advantages of using polynomials with a complex variable. We consider the propagation of a Gaussian pulse in a 1D cavity, $x \in [-2, 2]$, with absorbing boundary conditions at the endpoints $x = \pm 2$. Furthermore, we assume that $x = 0$ represents an interface between the two halves of the cavity and that each half is a different homogeneous material. For simplicity we assume the materials are nonmagnetic (i.e., $\mu_1 = \mu_2 = 1$) and the positive region is occupied by the vacuum (i.e., $\varepsilon_1 = 1$ if $x > 0$) while the remaining region is filled with a glass (i.e., $\varepsilon_2 = 4$ if $x \leqslant 0$). The exact time-domain solution of this problem can be found in [1,29]. At time $T = 0$ ns, the pulse is located at $x = 1$ (i.e., in the vacuum region) and propagates from right to left as shown on the left of Fig. 1. The computational domain, $[-2, 2]$, is discretized into non-uniform grid where the cell sizes of the glass region are twice finer than those of the vacuum region. The global grid contains 72 cells which corresponds to 6 points per wavelength. We stop the simulation when the excitation pulse goes through the material interface, i.e., at time $T = 5$ ns. We shall compare the exact solution with the results obtained by using the DG method combined with the Chebyshev time scheme (DG-CH scheme). The DG-CH scheme can be written as

$$\mathbb{Y}^{n+1} = \Phi(\tau)\mathbb{Y}^n, \quad \text{where } \Phi(\tau) = \sum_{m=0}^{\infty} i^m \epsilon_m J_m(\tau\|\mathcal{H}\|_2) T_m(\mathcal{H}_{sc}), \tag{18}$$

where $J_m(\cdot)$ is the mth order Bessel function of the first kind, $\epsilon_0 = 1$ and $\epsilon_m = 2$ for $m > 0$, $\mathcal{H}_{sc} = -i\mathcal{H}/\|\mathcal{H}\|_2$ is the scaled matrix, and $T_m(\mathcal{H}_{sc})$ are the Chebyshev polynomials of the first kind, defined by the three-term recurrence relation: $T_{m+1}(\mathcal{H}_{sc}) = 2\mathcal{H}_{sc}T_m(\mathcal{H}_{sc}) - T_{m-1}(\mathcal{H}_{sc})$, with $T_0(\mathcal{H}_{sc}) = I$ and $T_1(\mathcal{H}_{sc}) = \mathcal{H}_{sc}$. The series in Eq. (18) converges if $m = M > e\tau\|\mathcal{H}\|_2/2$, where M is the truncation order. The right graph of Fig. 1 displays results obtained by using interpolation orders $p = 2$ and $p = 6$, and integrated until final time with the time step $\delta t = 0.1$ ns. We can see that the DG-CH scheme leads to a large error in the vacuum region and the solution becomes less accurate when increasing p from $p = 2$ to $p = 6$. In order to

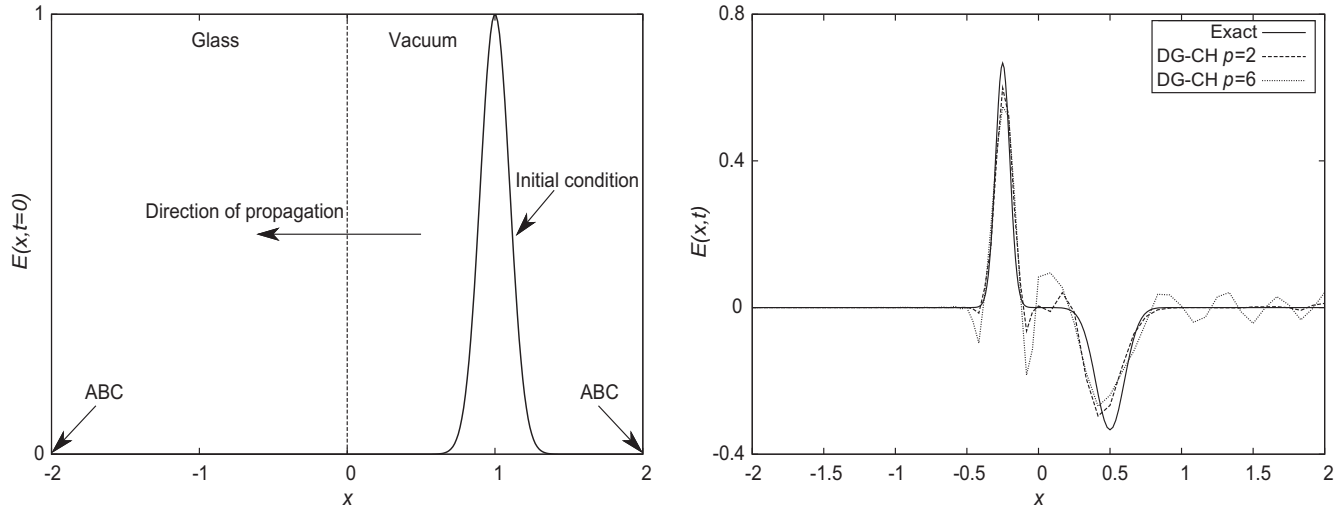

Fig. 1. On the left we plot the initial condition, $\boldsymbol{E}(x, t = 0) = \exp(-50(x-1)^2)$, of the Gaussian pulse in the 1D cavity with a material interface located at $x = 0$ and with Silver-Müller absorbing boundary conditions (ABC) at the endpoints $x = \pm 2$. The pulse propagates from the vacuum to glass regions. On the right we compare solutions for the $\boldsymbol{E}$-field component to the 1D Maxwell equation, computed using the DG-CH scheme when the pulse goes through the material interface. The solid line represents the exact solution while dashed and dotted lines are for DG-CH scheme with $p = 2$ and $p = 6$, respectively.

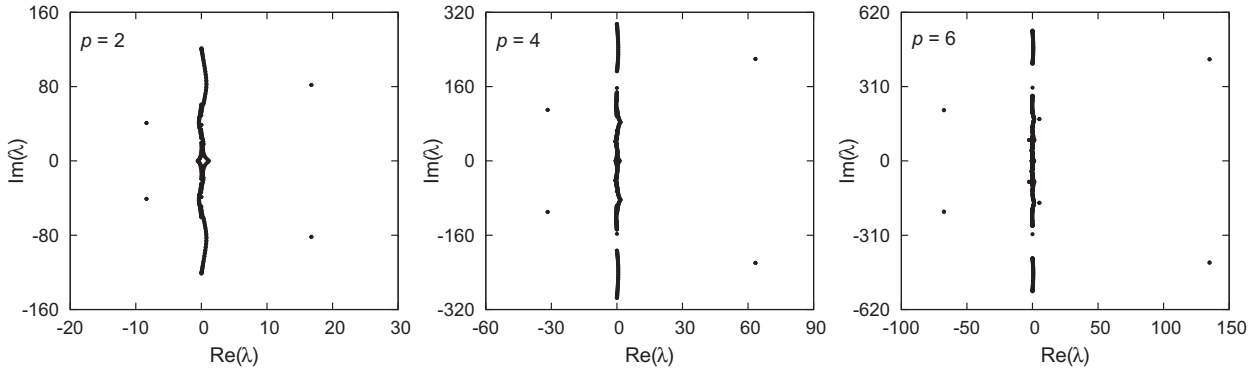

Fig. 2. Structure of the eigenvalue spectrum, λ, of the matrix $\mathcal{H}$ for $p = 2,\ 4,\ 6$ and absorbing boundary conditions.

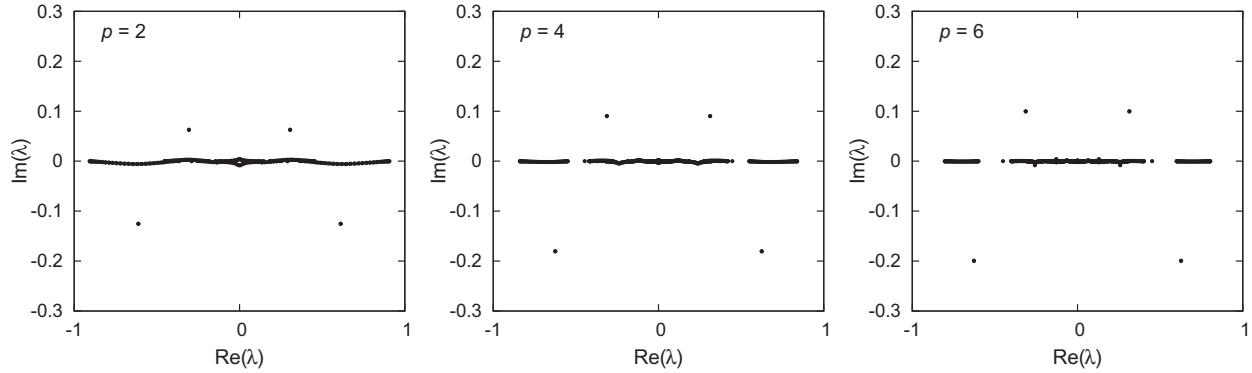

Fig. 3. Structure of the eigenvalue spectrum, λ, of the matrix $\mathcal{H}_{sc} = -i\mathcal{H}/\|\mathcal{H}\|_2$ for $p = 2,\ 4,\ 6$ and absorbing boundary conditions.

understand this loss of accuracy in the DG-CH scheme, we show in Fig. 2 the eigenvalue spectrum of the Hamiltonian matrix $\mathcal{H}$ for different p. We note in particular that the eigenvalues are distributed symmetrically with respect to the real axis. Note also that some of the eigenvalues, λ, are complex numbers with $\mathrm{Re}(\lambda) \neq 0$ and $\mathrm{Im}(\lambda) \neq 0$. Moreover the eigenvalues of $\mathcal{H}_{sc}$ all lie in the rectangle $[-1,1] \times [-a,b]$, where $a < 1$ and $b < 1$, as illustrated in Fig. 3. When applied the DG-CH scheme we need to calculate the matrix polynomial $T_m(\mathcal{H}_{sc})$ in Eq. (18). According to the spectral decomposition, Eq. (15), this can be accurately done if $T_m(\lambda_{sc})$ (where λ_{sc} is an eigenvalue of the matrix $\mathcal{H}_{sc}$) is well defined, which is not the case in the present example since the Chebyshev polynomial is applied to $\Re(\lambda_{sc})$ instead of λ_{sc}, which is not true if λ_{sc} is a complex number. Here, the evaluation of $\Phi(\tau)$ with Chebyshev polynomials for $M = e\tau\|\mathcal{H}\|_2/2$ leads to non-convergent results for all p. We have increased M by about 300% to obtain an accuracy of 10^{-2} and 10^{-1} for $p = 2$ and $p = 6$, respectively. To remedy this, we must use polynomials defined in the complex plane like Faber polynomials as described in the following sections and to modify the underlying scheme accordingly.

4.2. General aspects

Let G be a closed bounded continuum (not a single point) in the complex z-plane such that G^c, the complement of G, is simply connected in the extended z-plane and contains the point at infinity (e.g., a polygon, an ellipse, etc.). The Riemann mapping theorem asserts that there exists a conformal mapping $w = \Upsilon(z)$ which maps G^c onto $\{w : |w| > \rho\}$, the exterior of a closed disk of radius ρ in the w-plane, and satisfies the conditions $\Upsilon(\infty) = \infty$ and $\Upsilon'(\infty) = 1$ [30, Chapter 1, pp. 8–13]. The function $\Upsilon(z)$ has a Laurent expansion of the form

$$\Upsilon(z) = z + \sum_{m \geqslant 0} \beta_m z^{-m},$$

about the point at infinity. The constant ρ is called the logarithmic capacity or transfinite diameter of G. For a given positive integer m, the Faber polynomial of degree m, $F_m(z) = z^m + \ldots$, is obtained by deleting all negative powers of z from the corresponding Laurent expansion of $[\Upsilon(z)]^m$. Let $\Psi(w)$ be the inverse of $\Upsilon(z)$. Then $\Psi(w)$ maps the domain $\{w : |w| > \rho\}$ conformally onto G^c and has a Laurent expansion at infinity

$$\Psi(w) = w + \sum_{m \geqslant 0} \gamma_m w^{-m}, \tag{19}$$

where $\gamma_m = 1/\beta_m$. The family of Faber polynomials $\{F_m(z)\}_{m=0}^{\infty}$ associated with the conformal mapping $\Psi(w)$ can be defined by a generating function

$$\frac{\Psi'(w)}{\Psi(w) - z} = \sum_{m=0}^{\infty} \frac{F_m(z)}{w^{m+1}}, \quad |w| > \rho, \quad z \in G,$$

and satisfies the recurrence relation

$$F_{m+1}(z) = zF_m(z) - \sum_{j=0}^{m} \gamma_j F_{m-j}(z) - m\gamma_m, \quad m \geqslant 0, \quad F_0(z) = 1. \tag{20}$$

This formula is particularly useful for polygonal regions for which the expansion of Ψ may be obtained by means of the Schwarz-Christoffel transformation.

Any function $f(z)$ that is analytic inside G can be uniquely expanded into a series of Faber polynomials

$$f(z) = \sum_{m=0}^{\infty} c_m F_m(z), \quad z \in G, \tag{21}$$

where the coefficients c_m are called *Faber coefficients* with respect to G; they are defined as

$$c_m = \frac{1}{2\pi i}\int_{|w|=R}\frac{f(\Psi(w))}{w^{m+1}}dw, \quad R > \rho, \tag{22}$$

where the circle $C_R = \{w : |w| = R\}$ can be replaced by any closed rectifiable Jordan curve Γ_R such that $\Gamma_R \subset G^c \cup \{\infty\},\ z \in \Gamma_R$. In particular, we can choose Γ_R to be the image under $z = \Upsilon(w)$ of C_R. Here, the number R is chosen sufficiently small that f can be extended analytically to Γ_R. If Ψ can be extended continuously to C_ρ, then the value $R = \rho$ is also acceptable. We note that the Faber series, Eq. (21), converges uniformly and absolutely to f on every region bounded by Γ_R to which f can be extended analytically [30, pp. 108-112]. For some continuum G, one can get some special family of Faber polynomials. For instance, for the unit disk the Faber polynomial of degree m is z^m and the corresponding Faber series for an analytic function is its Taylor series about the origin. Multiples of the Chebyshev polynomials are the Faber polynomials for an ellipse with foci at $z = \pm 1$, and, in particular, for the real interval $[-1, 1]$. Full details of the theory of Faber polynomials and their approximating properties can be found in the standard books of Markushevich [30, Chap. 3] and Gaier [31, Chap. I] and the other important references cited there.

4.3. The Faber algorithm

Let Γ be the boundary of G. The Faber polynomial algorithm for solving the initial value problem in Eq. (9) is as follows. First, choose a Jordan curve Γ that encloses the spectrum of the Hamiltonian matrix $\mathcal{H}$. Next, find the corresponding conformal mapping Ψ. Finally, compute the Faber coefficients, $c_m(\tau)$, by means of Eq. (22) where $f(z) = \exp(\tau z)$. Once the coefficients $c_m(\tau)$ are evaluated, the discrete solution is calculated as

$$\mathbb{Y}^{n+1} = \sum_{m=0}^{\infty} c_m(\tau) F_m(\mathcal{H})\mathbb{Y}^n,$$

and the action of the Faber polynomials on $\mathbb{Y}^n$ is computed using the relation in Eq. (20) as

$$F_{m+1}(\mathcal{H})\mathbb{Y}^n = \mathcal{H}F_m(\mathcal{H})\mathbb{Y}^n - \sum_{j=0}^{m}\gamma_j F_{m-j}(\mathcal{H})\mathbb{Y}^n - m\gamma_m\mathbb{Y}^n. \tag{23}$$

However, this relation is, in general, unstable since the norm of the Faber polynomials growth rapidly with their orders, $\|F_m(z)\|_\infty \leqslant \rho^m V/\pi$ (see [32]). Here $\|\cdot\|_\infty$ denotes the uniform norm, $\|f\|_\infty = \max_{z\in G}|f(z)|$, and $V = \int_\Gamma |d\theta(z)| \geqslant 2\pi$, where $\theta(z)$ is the angle between the positive real axis and a tangent line to Γ. If G is convex, then $V = 2\pi$. To avoid this instability, the matrix $\mathcal{H}$ has to be scaled so that its spectrum lies inside the domain whose logarithmic capacity $\rho \leqslant 1$. If λ_F is the scaling factor, then $\exp(\tau\mathcal{H}) = \exp(\tilde{\tau}\mathcal{H}_{sc})$, where $\mathcal{H}_{sc} = \mathcal{H}/\lambda_F$ and $\tilde{\tau} = \lambda_F\tau$. The scaling factor λ_F should be chosen as small as possible to allow for larger time steps τ. In the following, we choose $\rho = 1$ and the curve Γ is taken to be an ellipse tightly enclosing the complex spectrum of $\mathcal{H}$. It is well known that, under these circumstances, the conformal mapping, $\Psi(w)$, in Eq. (19) is finite (i.e., it terminates) [30], and has the form

$$\Psi(w) = w + \gamma_0 + \gamma_1/w, \quad \gamma_1 \neq 0, \tag{24}$$

where $\gamma_0 = x_0 + iy_0$ is the center of the ellipse whose minor and major semi-axis $a = \rho + \gamma_1/\rho$ and $b = \rho - \gamma_1/\rho$, respectively. The logarithmic capacity of an ellipse is $\rho = (a + b)/2$. For $\rho = 1$, we have $\gamma_1 = 1 - b$ and $b = 2 - a$. Thus, the recursion relation for the Faber polynomials, Eq. (23), becomes

$$F_{m+1}(\mathcal{H}_{sc})\mathbb{Y}^n = (\mathcal{H}_{sc} - \gamma_0 I)F_m(\mathcal{H}_{sc})\mathbb{Y}^n - \gamma_1 F_{m-1}(\mathcal{H}_{sc})\mathbb{Y}^n, \quad m > 0, \tag{25}$$

where $F_0(\mathcal{H}_{sc})\mathbb{Y}^n = \mathbb{Y}^n$ and $F_1(\mathcal{H}_{sc})\mathbb{Y}^n = (\mathcal{H}_{sc} - \gamma_0 I)\mathbb{Y}^n$. Then the discrete solution is given by

$$\mathbb{Y}^{n+1} = \sum_{m=0}^{\infty} c_m(\tilde{\tau}) F_m(\mathcal{H}_{sc})\mathbb{Y}^n,$$

where the Faber coefficients can be solved analytically as

$$\begin{aligned} c_m(\tilde{\tau}) &= \frac{1}{2\pi i}\int_{|w|=1}\exp[\tilde{\tau}\Psi(w)]w^{-(m+1)}dw = \frac{1}{2\pi}\int_0^{2\pi}\exp[\tilde{\tau}\Psi(e^{i\theta})]e^{-im\theta}d\theta (w = e^{i\theta}) \\ &= \left(\frac{-i}{\sqrt{\gamma_1}}\right)^m \exp(\tilde{\tau}\gamma_0)J_m(2\tilde{\tau}\sqrt{-\gamma_1}). \end{aligned} \tag{26}$$

Here we have used the identity $\exp[z(s + a/s)/2] = \sum_{k=-\infty}^{\infty}(s/i\sqrt{a})^k J_k(i\sqrt{a}z),\ s,\ a \in \mathbb{C}$, and the Cauchy residue theorem to the contour integral involved. Note that, for the conformal mapping, Eq. (24), the Faber polynomials generated by Eq. (25) are related to Chebyshev polynomials of the first kind, $T_m(z)$, by $F_m(z) = 2(\gamma_1)^{m/2}T_m\big((z - \gamma_0)/\sqrt{4\gamma_1}\big), m \geqslant 1$.

Choice of the optimal ellipse. As we have already mentioned, the spectrum of the matrix $\mathcal{H}$ is symmetric with respect to the real axis. Hence, we set $y_0 = 0$. This spectrum lies in a rectangle $[\chi_1, \chi_2] \times [-\ell, \ell]$ with constants $\chi_{1,2}$ and ℓ to be determined

below. The strategy is to find an "optimal" ellipse that contains a scaled rectangle $[\chi_1^{sc}, \chi_2^{sc}] \times [-\ell^{sc}, \ell^{sc}]$, where $\chi_{1,2}^{sc} = \chi_{1,2}/\lambda_F$ and $\ell^{sc} = \ell/\lambda_F$.

Let $W(\mathcal{H})$ denote the field of values (or numerical range) of the matrix $\mathcal{H}$, that is, $W(\mathcal{H}) = \{z^\dagger \mathcal{H} z / z^\dagger z : z \in \mathbb{C}^n, z \neq 0\}$. Like the spectrum of a matrix, the field of values is a set that can be used to learn something about the matrix. In the case where $\mathcal{H}$ is nonnormal, $W(\mathcal{H})$ can give information that the spectrum alone cannot give. For a comprehensive overview of the theory of the field of values we refer to [33, Chap. 1]. Now we derive the bounds, $\chi_{1,2}$ and ℓ, for the field of values and the spectrum of $\mathcal{H}$ which is a non-Hermitian matrix. Any matrix $\mathcal{H}$ can be split into two Hermitian matrices as $\mathcal{H} = \Re(\mathcal{H}) + i\Im(\mathcal{H})$, where $\Re(\mathcal{H}) = (\mathcal{H} + \mathcal{H}^\dagger)/2$ and $\Im(\mathcal{H}) = (\mathcal{H} - \mathcal{H}^\dagger)/2i$. Then, the field of values of $\mathcal{H}$ is $W(\mathcal{H}) = W(\Re(\mathcal{H}) + i\Im(\mathcal{H}))$. Since the field of values of a Hermitian matrix is real, we have the following properties for the real and imaginary parts of the field of values of a non-Hermitian matrix [33, pp. 9-10]

$$\mathrm{Re}(W(\mathcal{H})) = W(\Re(\mathcal{H})) \quad \text{and} \quad \mathrm{Im}(W(\mathcal{H})) = W(\Im(\mathcal{H})).$$

Here Re and Im are used to denote the real and imaginary parts of a set, respectively. Hence, bounds on $W(\Re(\mathcal{H}))$ and on $W(\Im(\mathcal{H}))$ amount to a bounding box in the complex plane for $W(\mathcal{H})$. Since the spectrum of $\mathcal{H}$ is contained in $W(\mathcal{H})$, the same box gives bounds on the eigenvalues of $\mathcal{H}$

$$\lambda_{\min}^{\Re(\mathcal{H})} \leqslant \mathrm{Re}(\lambda^{\mathcal{H}}) \leqslant \lambda_{\max}^{\Re(\mathcal{H})} \quad \text{and} \quad \lambda_{\min}^{\Im(\mathcal{H})} \leqslant \mathrm{Im}(\lambda^{\mathcal{H}}) \leqslant \lambda_{\max}^{\Im(\mathcal{H})},$$

where $\lambda^{\mathcal{H}}$ is an eigenvalue of $\mathcal{H}$ and the subscripts min and max refers to a minimal and a maximal value, respectively. Moreover, since the matrix $\Im(\mathcal{H})$ has the form

$$\Im(\mathcal{H}) = -i\begin{pmatrix} 0 & \tilde{\mathbb{S}} \\ -\tilde{\mathbb{S}}^\dagger & 0 \end{pmatrix},$$

we have that $\lambda_{\min}^{\Im(\mathcal{H})} = -\lambda_{\max}^{\Im(\mathcal{H})}$. Then, we choose the parameters $\chi_{1,2}$ and ℓ as

$$\chi_1 = \lambda_{\min}^{\Re(\mathcal{H})}, \quad \chi_2 = \lambda_{\max}^{\Re(\mathcal{H})}, \quad \ell = \lambda_{\max}^{\Im(\mathcal{H})}. \tag{27}$$

The center of the ellipse coincides with that of the rectangle then $\gamma_0 = (\chi_1^{sc} + \chi_2^{sc})/2$. Since the vertices of the scaled rectangle lies in the ellipse, the following condition holds

$$\frac{b^2}{a^2} = \frac{b^2 - (\ell^{sc})^2}{c_{sc}^2}, \quad c_{sc} := \left|\frac{\chi_2^{sc} - \chi_1^{sc}}{2}\right|.$$

This condition gives a relation between b and the scaling factor λ_F.

Choice of the scaling factor. Let $\mathcal{F}_M$ be the Faber projection obtained by truncating the Faber series, i.e., $\mathcal{F}_M(f)(z) = \sum_{m=0}^{M} c_m F_m(z)$. The truncation order, M, can be determined by requiring that the Faber coefficients decay exponentially, e.g., for $M \geqslant e\tilde{\tau}$. The projection $\mathcal{F}_M$ is a bounded linear operator which satisfies $\mathcal{F}_M(p_M) = p_M$ for any polynomial p_M of degree M. The error bound for truncated Faber series is given by (see [32])

$$\|f - \mathcal{F}_M(f)\|_\infty = \frac{V}{\pi}\frac{(\rho/R)^{M+1}}{1-\rho/R}\max_{z\in\Gamma_R}|f(z)|.$$

In our experiments, G is an ellipse (which is convex $V = 2\pi$) with $\rho = 1$ and symmetric with respect to the real axis. For the exponential function it can be proved following [22] that

$$\|\exp - \mathcal{F}_M(\exp)\|_\infty = \frac{2}{e}\frac{1+\alpha}{\alpha}\exp[\tilde{\tau}(\gamma_0 + \mathcal{O}(1/M))]\left(\frac{e}{M}\right)^{M+1}, \quad M \geqslant 1+\alpha, \tag{28}$$

for any $\alpha > 0$. Hence, the Faber series converges exponentially as the truncated order M increases. To avoid the exponential growth of the factor $\exp[\tilde{\tau}(\gamma_0 + \mathcal{O}(1/M))]$ and to allow for larger time steps $\tau = \tilde{\tau}/\lambda_F$, the scaling factor λ_F must be minimal. The idea is to construct the minimum-area ellipse circumscribed to the scaled rectangle $[\chi_1^{sc}, \chi_2^{sc}] \times [-\ell^{sc}, \ell^{sc}]$ such that λ_F is minimal. One can show that the ellipse with center γ_0 and

$$\gamma_1 = \frac{\left(c_{sc}^{2/3} + \ell_{sc}^{2/3}\right)\left(c_{sc}^{4/3} - \ell_{sc}^{4/3}\right)}{4\rho}, \quad \rho = \frac{\sqrt{c_{sc}^2 + \left(\ell_{sc}c_{sc}^2\right)^{2/3}} + \sqrt{\ell_{sc}^2 + \left(c_{sc}\ell_{sc}^2\right)^{2/3}}}{2}, \tag{29}$$

is that circumscribed to the scaled rectangle with minimal area and smallest capacity [34]. Since $\rho = 1$, the smallest λ_F is reached when $b^2 = \ell_{sc}^2 + \left(c_{sc}\ell_{sc}^2\right)^{2/3}$, or

$$\frac{b}{a} = \left(\frac{\ell_{sc}}{c_{sc}}\right)^{2/3} = \left(\frac{\ell}{c}\right)^{2/3}, \quad c := \left|\frac{\chi_2 - \chi_1}{2}\right|.$$

Substituting $a = 2 - b$ in the above equation we find the scaling factor

$$\lambda_F = \frac{(\ell^{2/3} + c^{2/3})^{3/2}}{2}. \tag{30}$$

Finally, the Faber algorithm for approximating $\exp(\tau\mathcal{H})\mathbb{Y}^n$ is summarized in Algorithm 2.

Algorithm 2. Approximating $\exp(\tau\mathcal{H})\mathbb{Y}^n$ by Faber polynomials

input: the fixed time step τ
input: the matrix $\mathcal{H}$
1: Compute $\Re(\mathcal{H}) = (\mathcal{H} + \mathcal{H}^\dagger)/2$ and $\Im(\mathcal{H}) = (\mathcal{H} - \mathcal{H}^\dagger)/2i$
2: Compute $\chi_{1,2}$ and ℓ using Eq. (27)
3: Compute the scaling factor λ_F using Eq. (30)
4: Compute $\gamma_0 = (\chi_1 + \chi_2)/2\lambda_F$ and γ_1 using Eq. (29)
5: Compute the Faber coefficients $c_m(\tilde{\tau})$ using Eq. (26)
6: Choose the truncation order M, such that $M \geqslant e\lambda_F\tau$
7: $\boldsymbol{p}_0 = F_0(\mathcal{H}_{sc})\mathbb{Y}^n; \boldsymbol{p}_1 = F_1(\mathcal{H}_{sc})\mathbb{Y}^n$
8: $\boldsymbol{z}_1 = c_0(\tilde{\tau})\boldsymbol{p}_0 + c_1(\tilde{\tau})\boldsymbol{p}_1$
9: **for** $m = 1$ **to** $M - 1$ **do**
10: $\quad \boldsymbol{p}_{m+1} = \mathcal{H}_{sc}\boldsymbol{p}_m - \gamma_0\boldsymbol{p}_m - \gamma_1\boldsymbol{p}_{m-1}$
11: $\quad \boldsymbol{z}_{m+1} = \boldsymbol{z}_m + c_{m+1}(\tilde{\tau})\boldsymbol{p}_{m+1}$
12: **end for**
13: **return** $\boldsymbol{z}_M \approx \exp(\tau\mathcal{H})\mathbb{Y}^n$

5. Numerical results

In this section, we provide three numerical examples to illustrate the accuracy and capability of the Faber scheme developed in the previous section. For the last two examples, we compare the Faber scheme with the fourth-order leap-frog (LF_4) time scheme developed in [35]. The LF_4 scheme can be written as

$$\mathbb{Y}^{n+1} = \mathbb{Y}^{n-1} + 2\tau\mathbb{G}(\tau)\mathbb{Y}^n, \quad \text{where } \mathbb{G}(\tau) = \mathcal{H} + \tau^2\mathcal{H}^3/6.$$

The LF_4 scheme is stable if the time step satisfies $\tau \leqslant \left(2^{\frac{1}{3}} + 2^{\frac{2}{3}}\right)/\|\mathcal{H}\|_2 \simeq 2.847/\|\mathcal{H}\|_2$. The computational work of the LF_4 scheme per time step mainly consists of three matrix–vector products and the algorithm to compute $\mathbb{Y}^{n+1}$ involves the storage of four vectors $(\mathbb{Y}^{n-1}, \mathbb{Y}^n, \mathcal{H}\mathbb{Y}^n, \mathbb{Y}^\star = \mathbb{Y}^n + \mathcal{H}\mathbb{Y}^n)$.

5.1. Gaussian pulse propagation in an absorbing dielectric medium

We consider the example of the Gaussian pulse already treated in Subsection 4.1 and we apply the Faber propagation scheme associated with an elliptic contour. The time step is fixed to $\delta t = 1$ ns (i.e., $\tau = 0.3$ m) and the simulation time is $T = 5$ ns. In Fig. 4 we show the elliptic contours that contain the eigenvalue spectrum of the scaled Hamiltonian $\mathcal{H}_{sc} = \mathcal{H}/\lambda_F$ for $p = 2$ and $p = 6$. The truncation order, M, of the Faber polynomial approximation is set by the exponential decay of the Faber coefficients, c_m, in Eq. (26). Fig. 5 shows the behavior of $|c_m|$ (the modulus of c_m) together with the approximation error for the truncated Faber expansion, Eq. (28), as a function of M. The modulus of c_m is bounded by 1 and decays exponentially from $M = \tilde{\tau} = \lambda_F\tau$ on. The approximation error is constant until $M = \tilde{\tau}$ and then starts to decrease. The choice of M in the interval $[1.3\tilde{\tau}, 2\tilde{\tau}]$ gives an error which ranges in the interval $[10^{-10}, 10^{-15}]$. Taking more than $2\tilde{\tau}$ terms has no impact on improving the accuracy. In the present case, we use $M = 70$ for $p = 2$ and $M = 230$ for $p = 6$. In Fig. 6 we compare the exact solution for the $\boldsymbol{E}$-field with those obtained by the DG-Faber method. It is particularly noteworthy how much improvement there is in the accuracy of the phase error when increasing the order of approximation from $p = 2$ to $p = 6$.

5.2. Plane-wave scattering by a dielectric circular cylinder

As a more challenging problem, let us consider the scenario shown on Fig. 7 in which a plane wave with frequency F = 300 MHz impinges on a dielectric cylinder, experiencing reflection and refraction at the material interface. The problem is solved in a total field formulation [1]. The exact time-domain solution of this problem is given in [29, p. 666]. The cylinder has a radius of $r_0 = 0.6$ m and bounds a nonmagnetic material with a relative permittivity $\varepsilon_r = 8$. The surrounding medium is assumed to be vacuum, i.e., $\varepsilon_r = \mu_r = 1$. The computational domain Ω is bounded by a square of side length 3.2 m centered at (0,0). A Silver-Müller absorbing condition is applied on the boundary of the square. We use a fully bodyconforming grid with a total of 2527 vertices and 4896 elements, having an average edge length of 0.2 wavelength, as illustrated in Fig. 7. The physical simulation time has been set to 9 periods (T = 33 ns) of the incident wave. To ensure a proper representation of the curved boundaries, and to eliminate the geometrical error, we apply a high-order geometrical mapping for elements near the curvilinear boundaries while the interior elements are treated with affine mapping [27]. We compare the Faber scheme with the LF_4 scheme for different p. For the LF_4 scheme we use the maximum time step allowed by the stability condition which is given by $\delta t = \tau/c_0$ where $\tau = 2.847/\|\mathcal{H}\|_2$ with $\|\mathcal{H}\|_2 \approx 617,\ 2609,\ 4808,\ 8358$ for $p = 2,\ 3,\ 4,\ 5$, respectively. For the Faber scheme we fix the time step $\delta t = 1$ ns for all p then we calculate the truncation order $M = 1.3\tau\lambda_F$ where the scaling

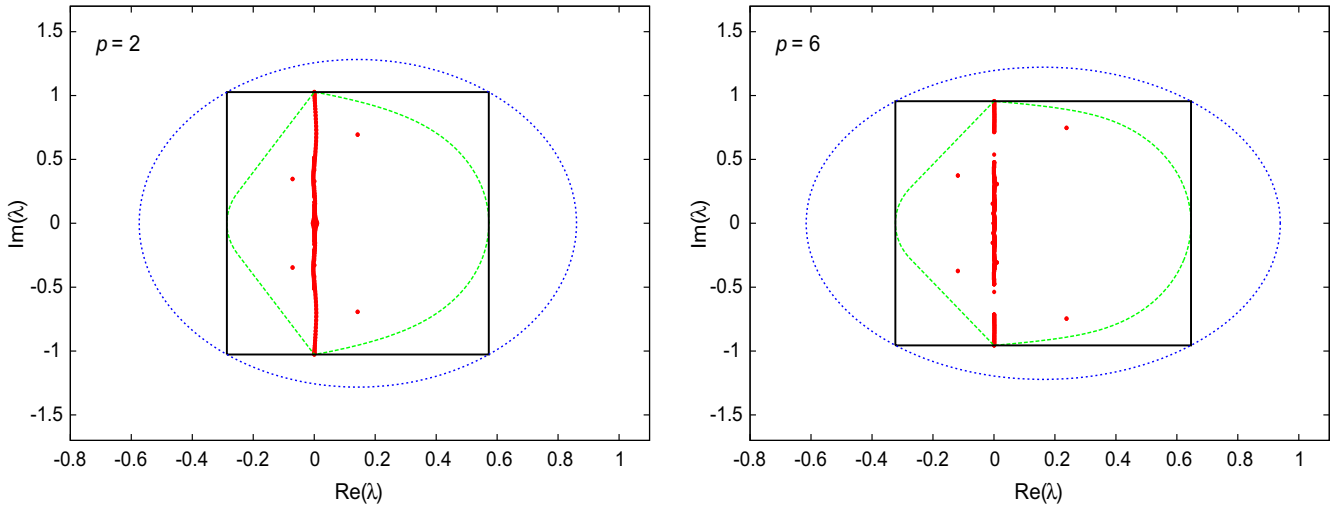

Fig. 4. We show the elliptic contour (dotted line) used in the simulation of the Gaussian pulse for $p = 2$ (left) and $p = 6$ (right). This contour circumscribes the scaled rectangle (solid line) that encloses the numerical range (dashed line) of the scaled Hamiltonian $\mathcal{H}_{sc} = \mathcal{H}/\lambda_F$ where $\lambda_F = 117.85$ for $p = 2$ and $\lambda_F = 568.44$ for $p = 6$. We can see that the numerical range gives bounds on the eigenvalues (filled circle), λ, of $\mathcal{H}_{sc}$. The logarithmic capacity is one, $\rho = 1$, and the corresponding conformal mapping, Eq. (24), reads $\Psi(w) = w + 0.1432 - 0.2827/w$ for $p = 2$ and $\Psi(w) = w + 0.1616 - 0.2224/w$ for $p = 6$.

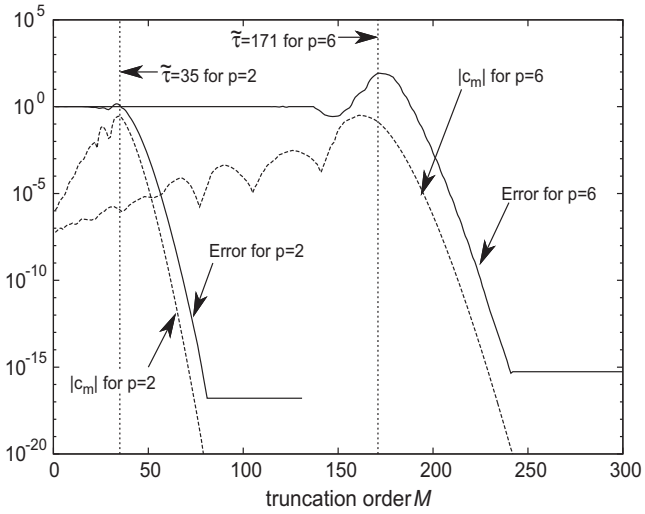

Fig. 5. The linear-log plot of the modulus of the Faber coefficients $|c_m|$ (dashed lines) and of the approximation error (solid lines), $\|\exp(\tau\mathcal{H}) - \sum_{m=0}^{M} c_m(\tilde{\tau}) F_m(\mathcal{H}_{sc})\|_\infty$, versus the truncation order M for $p = 2$ and $p = 6$. The vertical dotted lines represent the scaled time step $\tilde{\tau} = \lambda_F \tau$.

factor $\lambda_F \approx 379,\ 1601,\ 2950,\ 5128$ for $p = 2,\ 3,\ 4,\ 5$, respectively. Results are gathered in Table 1 in terms of accuracy and computational effort for simulations conducted on a Dell Precision M90 workstation equipped with an Intel Core processor and 2 GB of RAM. For a given p, the Faber scheme yields 1–3 orders of magnitude improvement in accuracy over the LF_4 scheme. The memory storage required by both schemes is similar while the Faber scheme requires almost 1.35 times less CPU time than the LF_4 scheme. This improvement in CPU time is due to the scaling factor λ_F being 1.6 times smaller than $\|\mathcal{H}\|_2$, which reduces the number of truncation order, M, in the Faber series. Furthermore, to achieve a given accuracy, the Faber scheme yields a considerable saving in computational effort. Careful inspection of the computational results in Table 1 confirms this. Finally, contour lines of the E_z component for numerical simulations performed with the LF_4 and Faber schemes, are illustrated in Fig. 8 using the interpolation order $p = 2$.

5.3. Exposure of human head tissues to a localized source radiation

As a final example, we consider the application of the Faber propagation scheme to the simulation of a considerably more challenging problem involving an irregularly shaped and heterogeneous medium with conductive materials. The problem under consideration is concerned with the propagation of an EM wave emitted by a localized source in a realistic geometrical model of head tissues. Starting from magnetic resonance images of the Visible Human 2.0 project [36], head tissues are segmented and the interfaces of a selected number of tissues are triangulated. Different strategies can be used in order to obtain

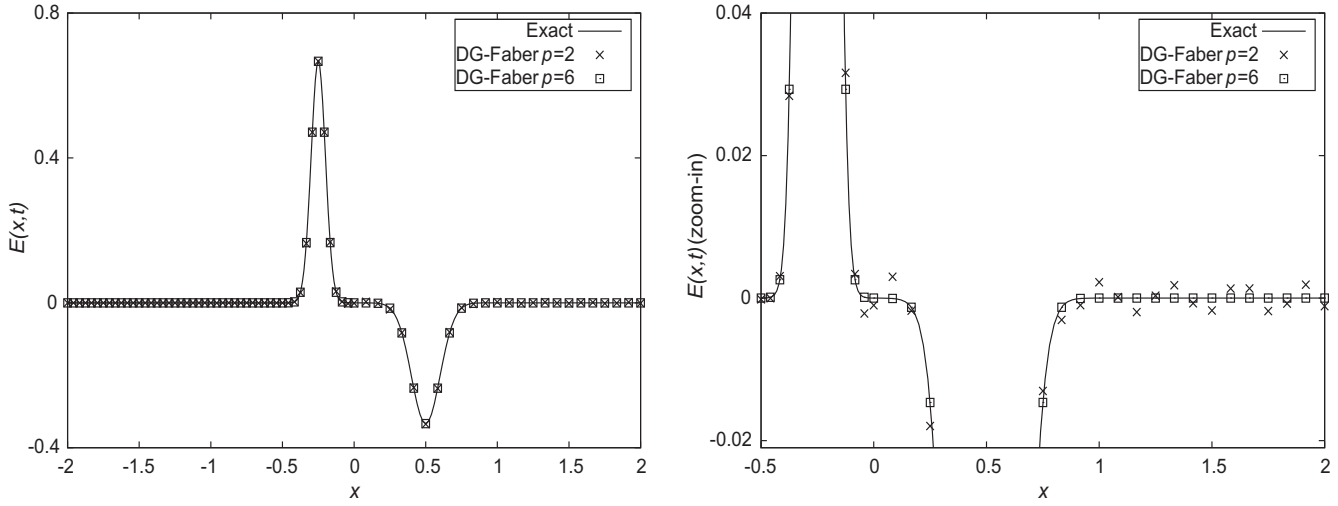

Fig. 6. We compare the exact solution (solid line) of the Gaussian pulse with solutions obtained using the DG method based on Faber polynomial integrator for $p = 2$ (cross) and $p = 6$ (square). On the right we show a zoom of the area $[-0.5, 2.0] \times [-0.02, 0.04]$. We note that the L^2 error between exact and DG solutions decreases from 4.93×10^{-3} for $p = 2$ to 3.6×10^{-5} for $p = 6$.

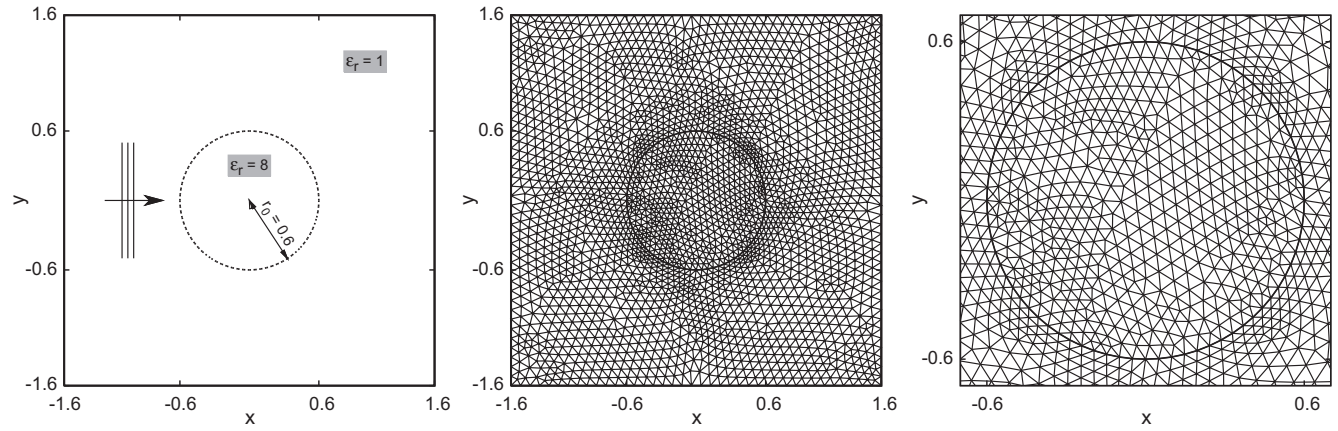

Fig. 7. Starting from the left, the computational domain and problem setup for the scattering example is depicted in the first graph. In the center is shown the finite element grid, consisting of 4896 triangles, used for computing scattering by a dielectric cylinder of size 0.6 m. A zoom of the boundary of the cylinder in the right figure illustrates the bodyconforming nature of the mesh.

Table 1
Computational effort and L^2-errors when the LF_4 and Faber time-stepping schemes are applied to the scattering problem with interpolation order p after integrating over time $T = 33$ ns. For each case, we give the number of matrix vector products (# matvecs), the CPU time (CPU) in minutes, and the memory usage (RAM) in Megabytes to achieve the final time period. For the Faber scheme, the CPU time also includes the time for computing the parameters given in lines 1–5 of Algorithm 2.

Scheme (p = 2)	δt (ns)	Error on ($\boldsymbol{E}$,$\boldsymbol{H}$)	# matvecs	CPU (min)	RAM (MB)
LF_4	1.538E-02	2.02E-02	6438	28	38.83
Faber	1.000E-00	1.63E-03	4851	20	39.91
Scheme (p = 3)	δt (ns)	Error on ($\boldsymbol{E}$,$\boldsymbol{H}$)	# matvecs	CPU (min)	RAM (MB)
LF_4	3.638E-03	2.75E-03	27216	197	91.72
Faber	1.000E-00	6.78E-05	20592	145	93.51
Scheme (p = 4)	δt (ns)	Error on ($\boldsymbol{E}$,$\boldsymbol{H}$)	# matvecs	CPU (min)	RAM (MB)
LF_4	1.974E-03	9.52E-04	50157	556	173.38
Faber	1.000E-00	2.53E-06	37950	413	176.07
Scheme (p = 5)	δt (ns)	Error on ($\boldsymbol{E}$,$\boldsymbol{H}$)	# matvecs	CPU (min)	RAM (MB)
LF_4	1.135E-03	5.12E-05	87192	1404	248.95
Faber	1.000E-00	8.56E-08	65967	1036	252.71

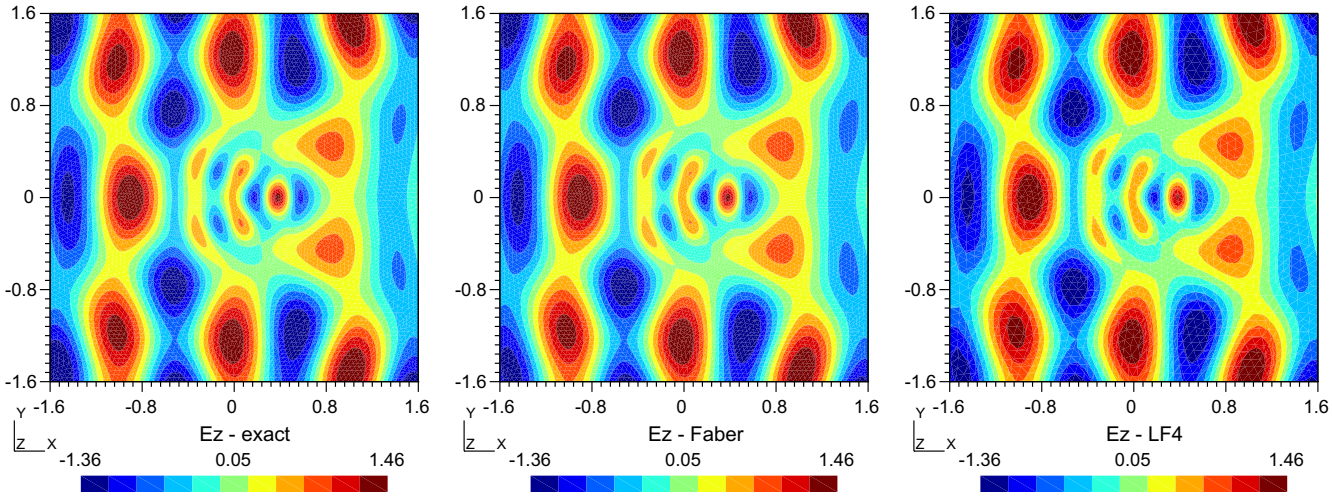

Fig. 8. Contour lines of E_z component for the exact solution (left) and for solutions resulting from the Faber (center) and LF_4 (right) schemes.

a smooth and accurate segmentation of head tissues and interface triangulations as well. The strategy adopted in this example consists in using a variant of Chew's algorithm [37], based on Delaunay triangulation restricted to the interface, which allows to control the size and aspect ratio of interface triangles. Example of triangulations of the skin and skull are shown in Fig. 9. Then, these triangulated surfaces together with a triangulation of the artificial absorbing boundary of the overall computational domain are used as inputs for the generation of volume meshes. Finally, the GHS3D tetrahedral mesh generator [38] is used to mesh the volume domains between the various interfaces. The exterior of the head must also be meshed, up to a certain distance from the skin. The computational domain is here artificially bounded by a sphere on which the Silver-Müller condition is imposed. Overall, the constructed geometrical model considered here consists of four tissues (skin, skull, CSF – Cerebro Spinal Fluid, brain) and the global tetrahedral mesh consists of 60,590 vertices and 361,848 tetrahedra. The minimum, maximum and average lengths of the mesh edges are equal to 1.85 mm, 45.37 mm and 11.36 mm, respectively. The characteristics of the tissues are summarized in Table 2 where the values of the relative permittivity ε_r, and the conductivity σ, correspond to a frequency F = 1800 MHz and have been obtained from a special purpose online data base. For all

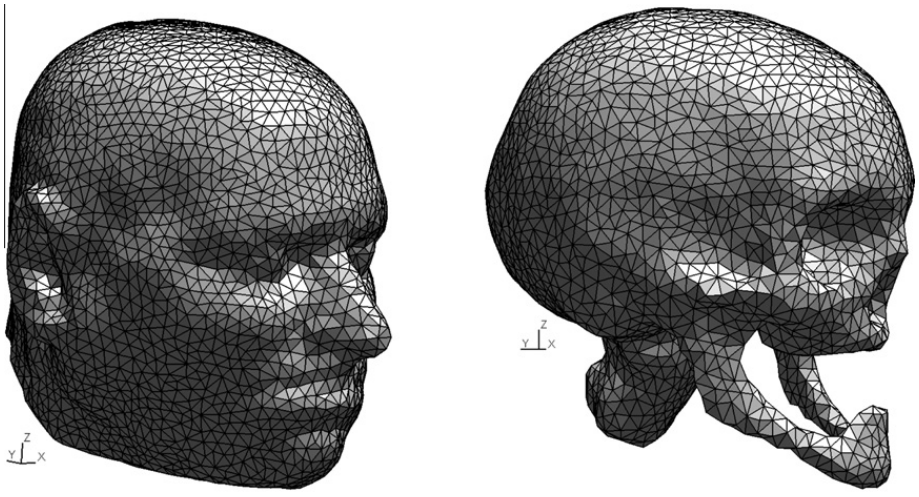

Fig. 9. Surface mesh of the skin (left) and the skull (right).

Table 2
Electromagnetic characteristics of the selected head tissues at frequency $F = 1800$ MHz.

Tissue	ε_r	σ (S/m)	Wavelength (mm)
Skin	38.87	1.18	26.73
Skull	15.56	0.43	42.25
CSF	67.20	2.92	20.33
Brain	43.55	1.15	25.26

tissues, the relative permeability, μ_r, is set to 1. Finally, a dipolar type source is localized near the right ear of the head yielding a current of the form $\boldsymbol{J}_z(\boldsymbol{x},t) = \delta(\boldsymbol{x}-\boldsymbol{x}_d)f(t)$, where $f(t)$ is a sinusoidally varying temporal signal and $\boldsymbol{x}_d$ is the localization point of the source. The physical simulation time has been fixed to five periods of the temporal signal. A discrete Fourier transform of the components of the electric field is computed during the last period of the simulation. Contour lines of the modulus of the electric field, $|\boldsymbol{E}|$, on selected planes of the skin for the approximate solutions resulting from the Faber and LF_4 schemes are visualized in Fig. 10 using the interpolation order $p = 2$. The Faber scheme produces a smoother solution around the right ear of the head (here the error between both solutions is about 10%). The time step used in the simulations are $\delta t = 0.00103$ ns for LF_4 scheme and $\delta t = 0.1$ ns for Faber scheme. The corresponding truncation order in the Faber

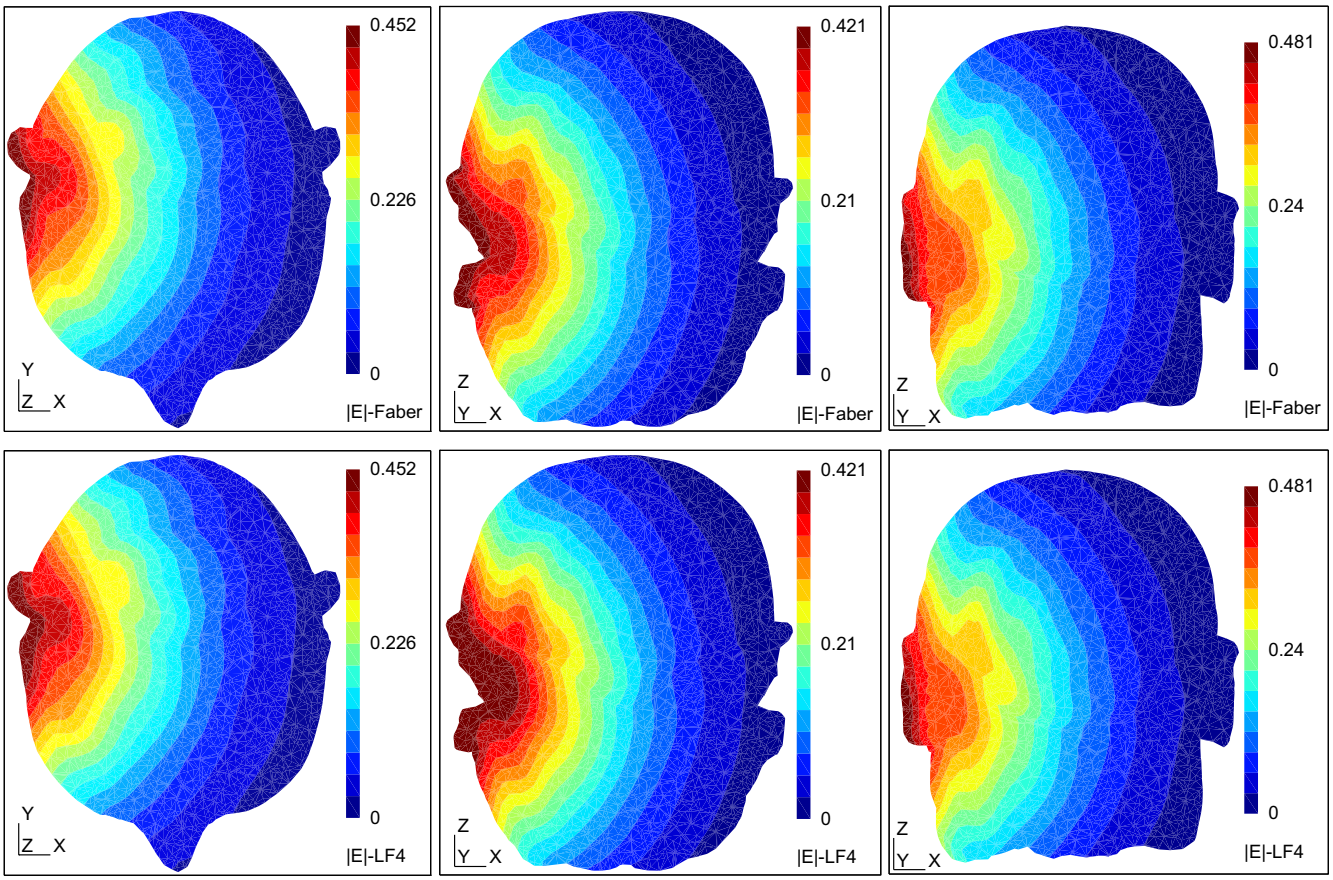

Fig. 10. Contour lines of the modulus of the electric field, $|\boldsymbol{E}|$, in selected cut planes of the head, using the Faber (top) and LF_4 (bottom) schemes.

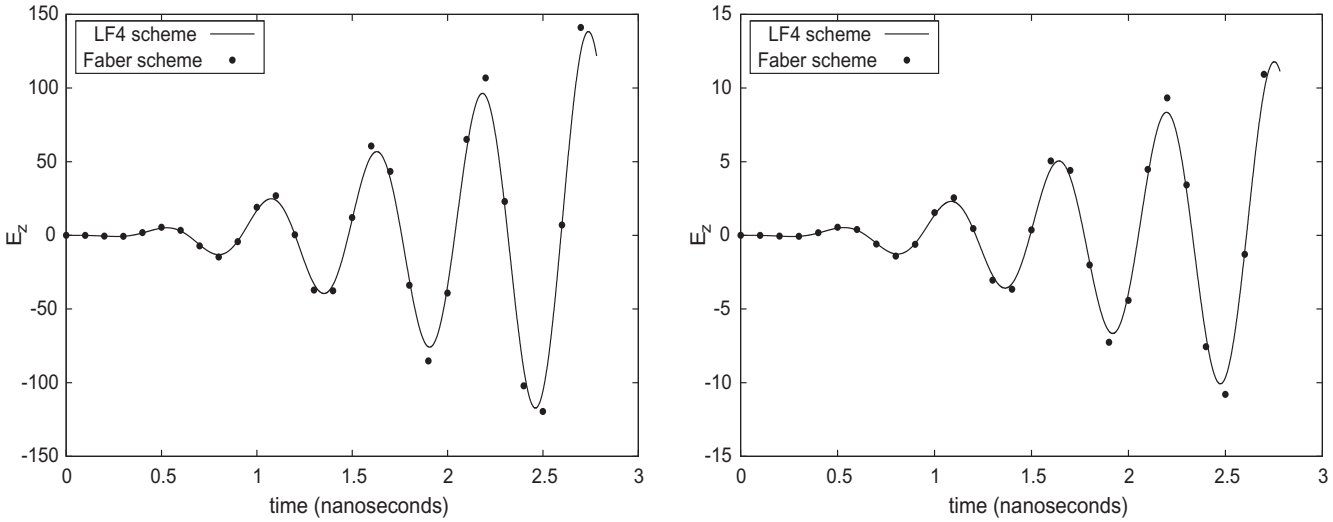

Fig. 11. Time evolution of the E_z component at selected points in free space (left) and in the brain (right).

expansion is chosen as $M = 1.3\tau\lambda_F$ with $\lambda_F \approx 5171$. For the sake of completeness, we compare in Fig. 11 the time evolution of the E_z component at two selected points in the free space near the ear and in the brain. With such comparisons, the advantage of the Faber scheme over the LF_4 scheme is more remarkable. Finally, we give some informations on the simulation times required by both schemes. On a workstation equipped with an Intel Xeon 2.33 GHz processor and 32 GB of RAM, the LF_4 scheme requires 10 h 18 min for a total of 2695 time steps, while the Faber scheme requires 6 h 31 min for a total of 28 time steps. We obtain that in this case the Faber scheme is 1.6 times less costly than LF_4 scheme for a given mesh. This gain could be larger since the LF_4 scheme would have required a very fine mesh or high-order interpolation order yielding a huge computation time to obtain the same kind of accuracy. We have run the LF_4 scheme on the same mesh for $p = 3$, the simulation time is 45 h 44 min for a total of 4826 time steps, and the error with the Faber solution is reduced to 3.7%.

6. Concluding remarks

We have continued the development of a new family of high-order time-stepping schemes for time-domain electromagnetics and discussed its properties and implementation in a high-order discontinuous Galerkin method. First, the discretized Maxwell equations are written in a Hamiltonian form. This leads to a time-continuous problem in the form of an initial-value problem for a system of first-order ODEs. Then the time integration method considered here is based on the expansion of the time evolution operator in a series of Faber polynomials. The proposed expansion is suitable for non-Hermitian Hamiltonian matrices, $\mathcal{H}$, and, hence, the proposed time integrator can handle absorbing media and conductive materials. The Faber algorithm consists of three ingredients. First, the choice of the optimal ellipse that encloses the spectrum of $\mathcal{H}$. Next, the calculation of the corresponding conformal mapping. Finally, the evaluation of the coefficients of the Faber series. We have implemented this algorithm in one, two and three space dimensions. The Faber scheme converges spectrally when increasing the polynomial degree. Compared to the fourth-order leap-frog scheme, the Faber method is more accurate and allows to reduce significantly the overall computing time and memory overhead. However, despite these encouraging results, some points still deserve to be addressed in order to improve the Faber algorithm. For instance, the optimization of the Jordan contour, Γ, that encloses the spectrum of $\mathcal{H}$. This should decrease the truncation order in the Faber expansion and consequently reduce the computational effort of the algorithm. In the present paper, Γ is chosen to be an ellipse since the associated Faber polynomials have the shortest (three-term) recurrence relation. This ellipse is obtained from the field of values of $\mathcal{H}$ which provides bounds of the eigenvalue. One should improve the bounds of the real part of the eigenvalues in order to obtain a tighter ellipse. Finally, it is worth pointing out that only the ohmic current term, $\sigma\boldsymbol{E}$, is considered in the Maxwell equations, Eq. (2). However, external currents such as time-dependent sources can also be handled by the Faber method, but this still requires further research. We plan to address these issues in future work.

Acknowledgments

This research was supported by the DGA (Direction Générale de l'Armement) under contract No. 2009.34.0010. This support is gratefully acknowledged. The author thanks Dr. Christophe Guiffaut (XLIM institute, Limoges, France) for his assistance during the process of this work. The author also wish to thank the associate editor and two anonymous referees for their constructive comments that helped to improve the manuscript.

References

[1] A. Taflove, S.C. Hagness, Computational Electrodynamics: The Finite-Difference Time-Domain Method, third ed., Artech House, Norwood, MA, 2005.
[2] S. Pernet, X. Ferrieres, G. Cohen, High spatial order finite element method to solve Maxwell's equations in time domain, IEEE Trans. Antennas Propag. 53 (9) (2005) 2889–2899.
[3] J.S. Hesthaven, T. Warburton, Nodal discontinuous Galerkin Methods: Algorithms, Analysis and Applications, Springer Texts Appl. Math., Springer-Verlag, Berlin, 2008.
[4] R.J. LeVeque, Finite Volume Methods for Hyperbolic Problems, Cambridge University Press, Cambridge, MA, 2002.
[5] J.S. Hesthaven, T. Warburton, Nodal high-order methods on unstructured grids. I. Time-domain solution of Maxwell's equations, J. Comput. Phys. 181 (1) (2002) 186–221.
[6] B. Cockburn, G.E. Karniadakis, C.W. Shu (Eds.), Discontinuous Galerkin methods. Theory, computation and applications, vol. 11 of Lecture Notes in Computational Science and Engineering, Springer-Verlag, Berlin, 2000.
[7] D. Sármány, M.A. Botchev, J.J.W. van der Vegt, Dispersion and dissipation error in high-order Runge–Kutta discontinuous Galerkin discretisations of the Maxwell equations, J. Sci. Comput. 33 (1) (2007) 47–74.
[8] J.G. Verwer, M.A. Botchev, Unconditionally stable integration of Maxwell's equations, Linear Algebra Appl. 431 (3-4) (2009) 300–317.
[9] V. Dolean, H. Fahs, L. Fezoui, S. Lanteri, Locally implicit discontinuous Galerkin method for time domain electromagnetics, J. Comput. Phys. 229 (2) (2010) 512–526.
[10] H. Fahs, High-order leap-frog based discontinuous Galerkin method for the time-domain Maxwell equations on non-conforming simplicial meshes, Numer. Math. Theor. Meth. Appl. 2 (3) (2009) 275–300.
[11] N.J. Higham, Functions of Matrices: Theory and Computation, SIAM, Philadelphia, 2008.
[12] H.A. De Raedt, J.S. Kole, K. Michielsen, M.T. Figge, Unified framework for numerical methods to solve the time-dependent Maxwell equations, Comput. Phys. Commun. 156 (1) (2003) 43–61.
[13] H.A. van der Vorst, An iterative solution method for solving $f(A)x = b$, using Krylov subspace information obtained for the symmetric positive definite matrix A, J. Comput. Appl. Math. 18 (2) (1987) 249–263.
[14] M. Min, P.F. Fischer, Scalable high-order algorithms for wakefield simulations, in: IPAC'10, Kyoto, Japan, 1865–1867, 2010.
[15] M. Tokman, Efficient integration of large stiff systems of ODEs with exponential propagation iterative (EPI) methods, J. Comput. Phys. 213 (2) (2006) 748–776.

[16] H. Tal-Ezer, R. Kosloff, An accurate and efficient scheme for propagating the time dependent Schrödinger equation, J. Chem. Phys. 81 (9) (1984) 3967–3971.
[17] C. Leforestier, R. Bisseling, C. Cerjan, M. Feit, R. Friesner, A. Guldberg, A. Hammerich, G. Jolicard, W. Karrlein, H.-D. Meyer, N. Lipkin, O. Roncero, R. Kosloff, A comparison of different propagation schemes for the time dependent Schrödinger equation, J. Comput. Phys. 94 (1) (1991) 59–80.
[18] A.E. Depristo, K. Haug, H. Metiu, A new method for calculating time-dependent quantum correlation functions for systems with many degrees of freedom, Chem. Phys. Lett. 155 (4-5) (1989) 376–380.
[19] H.A. De Raedt, K. Michielsen, J.S. Kole, M.T. Figge, Solving the Maxwell equations by the Chebyshev method: A one-step finite-difference time-domain algorithm, IEEE Trans. Antennas Propag. 51 (11) (2003) 3155–3160.
[20] J.S. Kole, Solving seismic wave propagation in elastic media using the matrix exponential approach, Wave Motion 38 (4) (2003) 279–293.
[21] J.B. Wang, J. Pan, Acoustical wave propagator with modified Chebyshev expansion, Comput. Phys. Commun. 174 (3) (2006) 187–190.
[22] I. Moret, P. Novati, The computation of functions of matrices by truncated Faber series, Numer. Funct. Anal. Optim. 22 (5-6) (2001) 697–719.
[23] Y. Huang, D.J. Kouri, D.K. Hoffman, General, energy–separable Faber polynomial representation of operator functions: Theory and application in quantum scattering, J. Chem. Phys. 101 (12) (1994) 10493–10506.
[24] A.G. Borisov, S.V. Shabanov, Wave packet propagation by the Faber polynomial approximation in electrodynamics of passive media, J. Comput. Phys. 216 (1) (2006) 391–402.
[25] W.T. Pollard, R.A. Friesner, Solution of the Redfield equation for the dissipative quantum dynamics of multilevel systems, J. Chem. Phys. 100 (7) (1994) 5054–5065.
[26] W. Huishinga, L. Pesce, R. Kosloff, P. Saalfrank, Faber and Newton polynomial integrators for open–system density matrix propagation, J. Chem. Phys. 110 (12) (1999) 5538–5547.
[27] H. Fahs, Improving accuracy of high-order discontinuous Galerkin method for time-domain electromagnetics on curvilinear domains, Int. J. Comput. Math. 88 (10) (2011) 2124–2153.
[28] R. Rieben, D. White, G. Rodrigue, High-order symplectic integration methods for finite element solutions to time dependent Maxwell equations, IEEE Trans. Antennas Propag. 52 (8) (2004) 2190–2195.
[29] C.A. Balanis, Advanced Engineering Electromagnetics, John Wiley & Sons, New York, 1989.
[30] A.I. Markushevich, Theory of Functions of a Complex Variable, vol. 3, Prentice-Hall, Englewood Cliffs, N.J., 1967.
[31] D. Gaier, Lectures on Complex Approximation, Birkhäuser Boston Inc., Cambridge, MA, 1987.
[32] S.W. Ellacott, Computation of Faber series with application to numerical polynomial approximation in the complex plane, Math. Comput. 40 (162) (1983) 575–587.
[33] R.A. Horn, C.R. Johnson, Topics in Matrix Analysis, Cambridge University Press, Cambridge, MA, 1991.
[34] B. Rublev, Y. Petunin, Minimum-Area ellipse containing a finite set of points. II, Ukrainian Math. J. 50 (8) (1998) 1253–1261.
[35] H. Fahs, S. Lanteri, A high-order non-conforming discontinuous Galerkin method for time-domain electromagnetics, J. Comput. Appl. Math. 234 (4) (2010) 1088–1096.
[36] P. Ratiu, B. Hillen, J. Glaser, D.P. Jenkins, Medicine Meets Virtual Reality 11 - NextMed: Health Horizon, vol. 11, chap. Visible Human 2.0 - the next generation, IOS Press, 275–281, 2003.
[37] L.P. Chew, Guaranteed-quality mesh generation for curved surfaces, in: Ninth Annual ACM Symposium Computational Geometry, ACM Press, 1993, pp. 274–280.
[38] P.-L. George, F. Hecht, E. Saltel, Automatic mesh generator with specified boundary, Comput. Methods Appl. Mech. Eng. 92 (3) (1991) 269–288.